Simultaneous 3-D Wireless Power Transfer to Multiple Moving Devices With Different Power Demands

Weiyi Tang, Qi Zhu, *Graduate Student Member, IEEE*, Jian Yang, *Member, IEEE*, Dongran Song, Mei Su, *Member, IEEE*, and Runmin Zou, *Member, IEEE*

***Abstract*—A real-time algorithm for simultaneous three-dimensional wireless power transfer to multiple moving devices with different power demands is proposed. An objective function of the weighted sum of the power transfer to the multiple moving devices is formulated. Devices with a more urgent need for charging will have higher weights. The objective function is optimized in real time. By the proposed algorithm, the wireless power transfer system transfers power as much as possible to the multiple devices based on their power demands so that the transfer distance is improved and charging time is saved. The proposed algorithm does not need to know the positions and orientations of the multiple moving devices, which is hard to be obtained in practice. The correctness and convergence of this algorithm are theoretically proved. The experimental results show that the proposed algorithm can adapt to both devices' movement and power demand variations. The convergence time of the proposed algorithm is 0.2 s when the devices' power demand urgencies change.**

***Index Terms*—Maximum power transfer, three-dimensional (3-D) space, wireless power transfer (WPT).**

I. Introduction

INDUCTIVE wireless power transfer (WPT) has evolved from an emerging technology to today's global billion-dollar industry [1]. Following the wide employment of WPT, there is an application scenario where the WPT powers personal mobile consumer electronics (such as mobile phones, smartwatches, tablets, and laptops). As shown in Fig. 1(a), the mobile phones, smartwatches, and other mobile consumer electronics are placed on the charging pad when being charged. This is not convenient, as people cannot use them freely during the charging process. The three-dimensional (3-D) WPT system, shown in Fig. 1(b), is designed to handle this problem. In this situation, people can freely use their electronics in the 3-D space when the devices are charged. Numerous studies have attempted to develop 3-D inductive WPT systems with wide-range ubiquitous magnetic field [2], [3] and omnidirectional powering [4], [5].

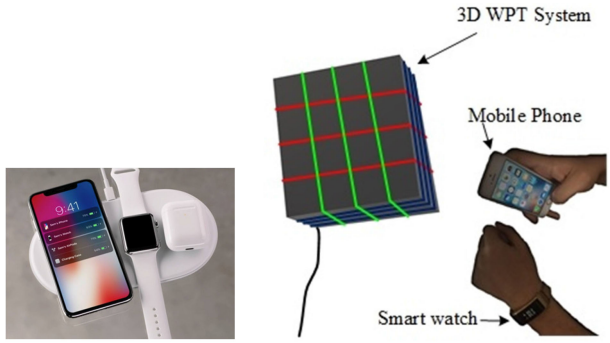

Fig. 1. (a) Current WPT systems require placing the mobile phones, smartwatches, and other mobile consumer electronics on the charging pad when charging. (b) Three-dimensional WPT system allows them moving around it when charging.

As a preliminary condition, the mobile device supporting WPT is equipped with one or more receiving (Rx) coils. In the case of multiple mobile devices, the multiple moving Rx coils must be charged regardless of their current positions and orientations. Besides, the orthogonal structure is chosen for the transmitting (Tx) coils of the WPT, since the mutual inductance between the Tx coils should be minimized and energy should not be exchanged between Tx coils. Otherwise, the transmission efficiency is reduced [6]. According to [4] and [5], the minimum physical dimensions of transmitting (Tx) and receiving (Rx) coils meeting the charging requirement can be categorized into the following three types of configurations.

1) Double orthogonal Tx coils and multiple double orthogonal Rx coils. This type of configuration is chosen and used in [1]–[5], [7]–[11]. By doing so, the volumetric coil structures are avoided on both Tx and Rx sides. When direct and quadrature (DQ) rotating magnetic-field-based Tx coil configuration is proposed for wireless charging of multiple devices in [2] and [3], the crossed dipole Tx and Rx coils configuration is proposed for wide-range 3-D omnidirectional inductive WPT in [4], [5], and [7]. By using a conductive magnetic shield to cancel out the magnetic flux generated from the lower coil segments,

Manuscript received May 25, 2019; revised August 7, 2019; accepted September 14, 2019. Date of publication September 17, 2019; date of current version February 11, 2020. This work was supported in part by the National Natural Science Foundation of China under Grant 51777217, in part by the Industrial Strong Base Engineering of China under Grant 0714-EMTC-02-0044, and in part by the China Scholarship Council under Grant 201706370068. Recommended for publication by Associate Editor O. Lucia. *(Corresponding author: Dongran Song.)*

The authors are with the School of Automation, Central South University, Changsha 410083, China (e-mail: 154601016@csu.edu.cn; csu_zhuqi@163.com; jian.yang@csu.edu.cn; humble_szy@163.com; sumeicsu@csu. edu.cn; rmzou@csu.edu.cn).

Color versions of one or more of the figures in this article are available online at http://ieeexplore.ieee.org.

Digital Object Identifier 10.1109/TPEL.2019.2942098

a new coreless Tx coil configuration is proposed for a wide-range ubiquitous inductive WPT in [8] and [9]. Besides, multiple Tx modules with the same size structure are proposed in [10] and [11] for a ubiquitous Wi-power zone, so that a number of electric devices can be simultaneously charged during operation.

2) Triple orthogonal Tx coils and multiple single Rx coils. This configuration is presented in [12]–[20], as the Rx side has the simplest configuration. Raval *et al.* [12]–[14] introduce a rotating magnetic field within the 3-D power zone. The proposed system includes a cubic power transfer primary window generated by a rotating magnetic flux flow path. In [15], the optimal design of the proposed quadrature-shaped pickup has been conducted in terms of the length and width of the central crossed structure of omnidirectional WPT systems.
3) Single Tx coil and multiple triple orthogonal Rx coils. This configuration is rarely used, as the complex Rx coil structure is hard to be employed by the mobile devices.

When the former two types of coil configurations have been widely employed, it is necessary to control the magnetic field toward a specific location, thereby increasing the energy transfer efficiency and reducing unnecessary energy leakage [17]. The current amplitude control method capable of generating a magnetic vector at a set of points evenly distributed on a spherical surface is explained in [18]. In [19] and [20], it is shown that the distributions of the total input power, load power, and the efficiency form surfaces of a revolution of Lemniscate of Bernoulli, when the 3-D omnidirectional system is driven by a rotating current vector. In [21], an active field orientation method is proposed to shape the magnetic flux so as to minimize the leakage flux by controlling the amplitude and phase angle of the magnetizing current. However, their works [17]–[21] are analyzed based on stationary devices, the movement and the power demand variations of the devices are not taken into account.

According to the above-mentioned analysis, this article focuses on meeting four requirements to charge the multiple moving devices in 3-D space in the software side.

1) First, the WPT can transfer power as much as possible to the multiple devices so that the transfer distance is improved, and the charging time is saved.
2) Second, each device can be charged based on its power demand urgency, as the priority of being charged among multiple devices may be different. For instance, some Rx coils need to be charged right now, while others do not.
3) Third, the first two requirements above should be satisfied when the multiple devices are moving.
4) Fourth, the first two requirements above should also be satisfied quickly after the devices' power demand urgencies change.

In order to meet the four requirements, this article presents an algorithm to determine the real-time amplitude and phase differences of the Tx coil currents that supports charging multiple moving devices with different power demands. The overview of the proposed algorithm is summarized as follows.

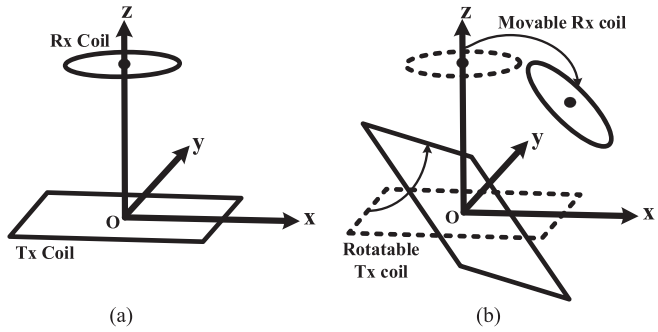

Fig. 2. (a) Spatial structure of traditional WPT system. (b) Rotatable Tx coil and movable Rx coil.

1) The mathematical description of the first two requirements mentioned above is established (see Section IV). An objective function with respect to the amplitude and phase differences of the Tx coil currents is formulated. The objective function is based on the weighted sum of the power transfer to the multiple moving devices. Optimizing the objective function in real time will satisfy the first two requirements.
2) A real-time algorithm is proposed to find out the real-time optimal amplitude and phase differences of the Tx coil currents (see Section V-A). The optimal solutions are found out based on the gradient of the objective function. The proof of the correctness and convergence is presented (see Section V-B).

Since the proposed algorithm is based on real-time optimization, it can adapt to the movement and the power demand variations of the devices. The experimental verification of the adaption is described in Section VI. It is also worth mentioning that all the calculations in the proposed algorithm are independent of positions and orientations of the multiple moving devices, which are difficult to obtain in practice.

The rest of the article is organized as follows. In Section II, the triple orthogonal Tx coil current control principle and its motivation are presented. In Section III, the mathematical modeling of the 3-D WPT system with the triple orthogonal Tx coils and multiple single Rx coils configuration is derived. In Section IV, the mathematical description of the objective function is presented. In Section V, a real-time algorithm for the maximum weighed sum of the power transfer to the Rx coils is proposed, and the correctness and convergence of the proposed algorithm are proved. In Section VI, an experimental prototype is displayed, and experimental verification of the proposed algorithm is presented.

II. Triple Orthogonal Tx Coil Current Control Principle and Its Motivation

As shown in Fig. 2(a), the spatial structure of traditional WPT system is usually a single Tx coil with a single Rx coil. In such a spatial structure, if the Rx coil is allowed to move in 3-D space, it is better that the Tx coil is also allowed to rotate. As shown in Fig. 2(b), if the Tx coil rotates following the Rx coil's movement, the leakage flux could be reduced, and the power

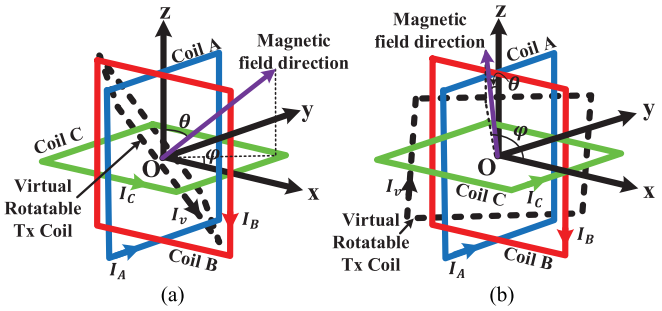

Fig. 3. Three orthogonal Tx coils and virtual rotatable Tx coil (a) both θ and $\varphi$are equal to $\pi/4$ (b) θ is equal to $\pi/4$, while φ is equal to $3\pi/4$.

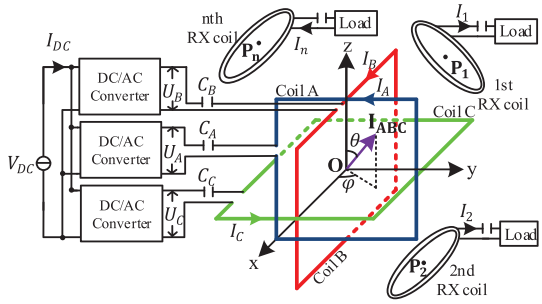

Fig. 4. Spatial structure of the triple orthogonal Tx coils with single Rx coil configuration with n moving Rx coils

transfer efficiency could be improved. However, rotating the Tx coil needs additional mechanical devices.

As shown in Fig. 3, in 3-D WPT system, the single Tx coil is replaced by three orthogonal coils. The three Tx coils A, B, and C are marked in blue, red, and green, respectively. The currents of the three Tx coils are, respectively, denoted as I_A, I_B, and I_C, which are complex numbers. The amplitude of the complex numbers represents the rms of the ac current, while the angle differences between the complex numbers represent the phase differences between the ac current.

Following [18] and [20], the amplitude and phase differences of the three currents in the three orthogonal Tx coils are regulated in spherical coordinate as

$$\mathbf{I_{ABC}} = I_{\text{base}}\mathbf{A}^T \tag{1}$$

where

$$I_{\mathbf{ABC}} = \begin{bmatrix} I_A & I_B & I_C \end{bmatrix}^T$$
$$\mathbf{A} = \begin{bmatrix} \sin\theta\cos\varphi & \sin\theta\sin\varphi & \cos\theta \end{bmatrix}.$$

I_{base} is the amplitude of the current vector in the spherical coordinate. θ and φ represent the polar and azimuthal angle in the spherical coordinate, respectively. To define a unique set of spherical coordinates for each point, θ and φ are restricted as $\theta \in [0, \pi]$ and $\varphi \in [0, 2\pi)$. The imaginary part of the three currents is regulated to be zero, which means the phases differences between the three current are 0° or 180°.

The motivation for the current control principle in (1) is imitating a rotatable Tx coil shown in Fig. 2(b), whose orientation is controllable. If the three Tx coil currents are regulated as (1), according to Biot–Savart law, the synthetic magnetic field vector at $\mathbf{O}$ is

$$\mathbf{B_O} = \frac{4N_{\text{turns}}\mu_0}{\sqrt{2}\pi l_{\text{square}}}\mathbf{I_{ABC}} \tag{2}$$

where N_{turns} is the number of turns of Tx coils, l_{square} is the length of a side of Tx coils, and μ_0 is the vacuum permeability. The amplitude is in direct proportion to I_{base}. The direction is controlled by θ and φ. The magnetic field direction is marked in purple in Fig. 3. According to (2), the synthetic magnetic field vector looks as if it is generated by a virtual rotatable square Tx coil, which is depicted with dashed line in Fig. 3, which is perpendicular to $\mathbf{B_O}$. The current of the virtual Tx coil I_v is equal to I_{base}. The numbers of turns and length of a side of virtual Tx coil are N_{turns} and l_{square}. Two examples are shown in Fig. 3. In Fig. 3(a), both θ and φ are equal to $\pi/4$. In Fig. 3(b), θ is equal to $\pi/4$, while φ is equal to $3\pi/4$.

Then, with the current control principle (1), the three orthogonal Tx coils look like a virtual rotatable Tx coil, whose orientation is controlled by θ and φ, and provide omnidirectional magnetic field in 3-D space.

Remark 1: The advantage of regulating the imaginary part of $\mathbf{I_{ABC}}$ to be zero is that, according to (2), the magnetic field can be shaped at a controllable specific direction, which is controlled by θ and φ. Otherwise, $\mathbf{B_O}$ is not a real vector and the magnetic field will rotate automatically and repeatedly in 3-D space. This may cause EMI issues for other devices. Meanwhile, regulating the imaginary part of $\mathbf{I_{ABC}}$ to be zero can reduce the variables that need to be controlled, while the synthetic magnetic field vector is still omnidirectionally controllable. This can reduce computational complexity and provide an advantage for the real-time control.

Remark 2: It needs to be clarified that it is not necessary to regulate the imaginary part of $\mathbf{I_{ABC}}$ to be zero in (1). Regulating the imaginary part of $\mathbf{I_{ABC}}$ to be zero may limit the power transfer capability of the system. The imaginary part of $\mathbf{I_{ABC}}$ represents extra degrees of freedom, and there are some other choices that are more beneficial, which should be studied further.

III. Mathematical Modeling of 3-D WPT System With Triple Orthogonal Tx and Multiple Single Rx Coils

Fig. 4 shows the spatial structure of the triple orthogonal Tx coils with single Rx coil configuration with n moving Rx coils. N Rx coils around the system are concerned in this article, while only three Rx coils are painted to represent multiple moving Rx coils. Table I lists the symbolic representation of electronic components in the 3-D WPT system.

Commonly, the mutual inductance is a positive variable. However, in this article, the meaning of mutual inductance is generalized, and it could be a positive or negative variable. The advantage is that modeling of the rotatable Rx coils needs only one uniform equation, otherwise it needs different equations when the Rx coils are with different orientations. An example is presented in Appendix I.

TABLE I
SYMBOLIC REPRESENTATION OF ELECTRONIC COMPONENTS

Symbol	Quantity
I_A, I_B, I_C, I_n	Current of Tx coil A, B, C, and *n*th Rx coil
U_A, U_B, U_C	Voltage source of Tx coil A, B, and C
L_A, L_B, L_C, L_n	Self-inductance of Tx coil A, B, C, and *n*th Rx coil
R_A, R_B, R_C	Coil resistance of Tx coil A, B, and C
R_{coiln}, R_n	Coil and load resistances of the *n*th Rx coil
C_A, C_B, C_C, C_n	Resonant capacitance of Tx coil A, B, C, and *n*th Rx coil
$M_{An}, M_{Bn}\ M_{Cn}$	Mutual inductance between coil A and *n*th Rx coil, coil B and *n*th Rx coil, and coil C and *n*th Rx coil
$M_{AB}, M_{BC}\ M_{AC}$	Mutual inductance between coil A and B, coil B and C, and coil A and C
M_{nm}	Mutual inductance between *m*th and *n*th Rx coil.

The amplitude and phase differences of I_A, I_B, and I_C can be independently regulated by their respective controllable voltage sources U_A, U_B, and U_C. U_A, U_B, and U_C are generated independently by their respective dc/ac converters powered by a dc voltage source.

Mutual inductances exist between Tx and Rx coils. There are also inductive couplings between the different moving Rx coils. Both the mutual inductances vary as the Rx coils move. The equivalent mathematical circuit model of the WPT system with the moving Rx coils can be described as

$$\begin{bmatrix} \mathbf{Z_{ABC}} & \mathbf{M} \\ \mathbf{M}^T & \mathbf{Z_N} \end{bmatrix} \begin{bmatrix} \mathbf{I_{ABC}} \\ \mathbf{I_N} \end{bmatrix} = \begin{bmatrix} \mathbf{U_{ABC}} \\ \mathbf{U_N} \end{bmatrix} \tag{3}$$

where

$$\mathbf{I_N} = \begin{bmatrix} I_1 & \cdots & I_N \end{bmatrix}^T \quad \mathbf{U_{ABC}} = \begin{bmatrix} U_A & U_B & U_C \end{bmatrix}^T$$

$$\mathbf{U_N} = \begin{bmatrix} 0 & \cdots & 0 \end{bmatrix}^T \quad \mathbf{M} = j\omega \begin{bmatrix} M_{A1} & \cdots & M_{AN} \\ M_{B1} & \cdots & M_{BN} \\ M_{C1} & \cdots & M_{CN} \end{bmatrix}$$

$$\mathbf{Z_{ABC}} = \begin{bmatrix} R_A + jX_A & j\omega M_{AB} & j\omega M_{AC} \\ j\omega M_{AB} & R_B + jX_B & j\omega M_{BC} \\ j\omega M_{AC} & j\omega M_{BC} & R_C + jX_C \end{bmatrix}$$

$$\mathbf{Z_N} = \begin{bmatrix} R_{\text{coil}1} + R_1 + jX_1 & \cdots & j\omega M_{1N} \\ \vdots & \ddots & \vdots \\ j\omega M_{1N} & \cdots & R_{\text{coil}N} + R_N + jX_N \end{bmatrix}$$

$$X_A = \omega L_A - 1/(\omega C_A) \quad X_B = \omega L_B - 1/(\omega C_B)$$

$$X_C = \omega L_C - 1/(\omega C_C) \quad X_n = \omega L_n - 1/(\omega C_n).$$

IV. MATHEMATICAL DESCRIPTION OF THE OBJECTIVE FUNCTION

In order to save the charging time and increase the transfer distance, the sum of the power transfer to each device should be maximized. To transfer power based on the devices' power demand urgencies, the sum is weighted. By doing so, the devices with a more urgent need for charging will have higher weights. The weighed sum of the power transfer to each device could be considered as a function with respect to the amplitude and phase differences of the Tx coil currents, when affected by the movement and power demand variation of the devices. The amplitude and phase differences of the Tx coil currents should be controlled to maximize the weighted sum of the power transfer in real time so that the WPT system can charge the multiple moving devices based on their power demand urgencies. Based on the above discussions, the weighted sum of power transfer is described by

$$P_w(\mathbf{I_N}) = w_1 P_1 + \cdots + w_N P_N = \mathbf{I_N^* R I_N} \tag{4}$$

where $P_n = I_n^* R_n I_n$, $\mathbf{R} = \text{diag}(w_1 R_1, w_2 R_2, \ldots, w_N R_N)$, and diag() indicates a diagonal matrix. P_n is the power transfer to the *n*th Rx coil. w_n represents the power allocation weight of the *n*th Rx coil. A larger w_n means that the *n*th receiver has a higher power demand urgency. Each Rx side will inform the WPT system of its power demand urgency u_n via wireless communication. The power demand urgency u_n is a limited nonnegative integer, and the WPT system assigns the power allocation weight w_n to each individual device based on u_n as

$$w_n = u_n / \sum_1^N u_n. \tag{5}$$

According to (3), $\mathbf{I_N}$ is described by$\mathbf{I_{ABC}}$ as

$$\mathbf{I_N}(\mathbf{I_{ABC}}) = -\mathbf{Z_N^{-1} M^T I_{ABC}}. \tag{6}$$

According to (4) and (6), the weighted sum of power transfer P_w can be denoted by

$$P_w(\mathbf{I_{ABC}}) = \mathbf{I_{ABC}^*}(\mathbf{Z_N^{-1} M^T})^* \mathbf{R Z_N^{-1} M^T I_{ABC}}. \tag{7}$$

Since $(\mathbf{Z_N^{-1} M^T})^* \mathbf{R Z_N^{-1} M^T}$ is Hermitian, and $\mathbf{I_{ABC}}$ is regulated as a real-number vector according to (1), the imaginary part of $(\mathbf{Z_N^{-1} M^T})^* \mathbf{R Z_N^{-1} M^T}$ is eliminated as

$$P_w(\mathbf{I_{ABC}}) = \mathbf{I_{ABC}^T R_e I_{ABC}} \tag{8}$$

where $\mathbf{R_e} = \text{Re}((\mathbf{Z_N^{-1} M^T})^* \mathbf{R Z_N^{-1} M^T})$ and Re() indicates the real part of the matrix. According to (1) and (8), P_w can be expressed as a function of θ and φ as

$$P_w(\theta, \varphi) = I_{\text{base}}^2 \mathbf{A R_e A}^T. \tag{9}$$

The two requirements described in Section I can be satisfied by optimizing (9) with respect to θ and φ, which can be described as an optimization problem as

$$\begin{cases} \underset{\theta,\varphi}{\text{maximize}} & P_w(\theta, \varphi) = I_{\text{base}}^2 \mathbf{A R_e A}^T \\ \text{subject to} & \theta \in [0, \pi], \varphi \in [0, 2\pi). \end{cases} \tag{10}$$

Since $\mathbf{R_e}$ is a positive real symmetric matrix, $\mathbf{R_e}$ is an orthogonal diagonalized as

$$\mathbf{R_e} = \mathbf{Q \lambda Q}^T \tag{11}$$

where $\mathbf{Q} = [\mathbf{Q_1}\ \mathbf{Q_2}\ \mathbf{Q_3}]$ and $\boldsymbol{\lambda} = \text{diag}(\lambda_{\max}, \lambda_{\text{mid}}, \lambda_{\min})$. $\mathbf{Q_1}$, $\mathbf{Q}_2$, and $\mathbf{Q}_3$ are the orthonormal basis. $\lambda_{\max}$, λ_{mid}, and $\lambda_{\min}$ are the maximum, intermediate value, and minimum of

the eigenvalue, respectively. Thus, the maximum weighted sum of power transfer is equal to $\lambda_{\max} I_{\text{base}}^2$, when

$$\mathbf{A}^T = \mathbf{Q_1} = \arg\max_{\theta,\varphi} P_w(\theta, \varphi). \tag{12}$$

V. Optimize the Objective Function in Real Time

A. Proposed Real-Time Algorithm

In this section, a real-time algorithm is proposed to solve the optimization problem (10) based on the gradient ascent method. In other words, the best magnetic field directions $\theta(t)$ and $\varphi(t)$ are found out to maximize P_w, and the latter can be obtained from wirelessly communicating with the Rx coils.

$\theta(t)$ and $\varphi(t)$ will evolve based on the gradients of the objective function as

$$\frac{d}{dt}\begin{bmatrix}\theta\\ \varphi\end{bmatrix} = k\begin{bmatrix}\partial P_w/\partial\theta\\ \partial P_w/\partial\varphi\end{bmatrix} \tag{13}$$

where k is a positive constant and represents the step size. In practice, the partial derivative of P_w can be implemented as

$$\partial P_w/\partial\theta = \left(P_w\left(\theta(t)+\Delta\theta, \varphi(t)\right) - P_w\left(\theta(t), \varphi(t)\right)\right)/\Delta\theta \tag{14}$$

$$\partial P_w/\partial\varphi = \left(P_w\left(\theta(t), \varphi(t)+\Delta\varphi\right) - P_w\left(\theta(t), \varphi(t)\right)\right)/\Delta\varphi. \tag{15}$$

Then, θ and φ can be updated as

$$\theta(t+1) = \theta(t) + \Delta T k(\partial P_w/\partial\theta) \tag{16}$$

$$\varphi(t+1) = \varphi(t) + \Delta T k(\partial P_w/\partial\varphi) \tag{17}$$

whereΔT is the control loop time. Equations (16) and (17) are independent of the positions and orientations of the multiple moving devices that are difficult to obtain in practice. Hence, the proposed algorithm does not need to know this information and brings convenience for engineering applications. Meanwhile, the current reference of Tx coils will be obtained as

$$\left[I_A^{\text{ref}}\ I_B^{\text{ref}}\ I_C^{\text{ref}}\right]^T = I_{\text{base}}\mathbf{A}^T. \tag{18}$$

The block diagram of the full algorithm is presented in Fig. 5. $\Delta\theta$ and $\Delta\varphi$ should be sufficiently small so that the WPT system will not cause large chattering around the optimization points. They should also be set sufficiently big so that the sensors can sense their changes. There is also a tradeoff when setting the value of step size *k*. It should be set sufficiently small so that the WPT system will not cause large chattering around the optimization points and sufficiently big to fasten the convergence time response performance to the movement and the power demand variation of the devices. In numerical optimization, line search methods [22] are usually used to decide the value of the step size *k*. Typical line search methods try out a sequence of candidate values for step size *k,* stopping to accept one of these values when certain conditions are satisfied. The objective function is assumed to be known and unchanged. It can be calculated by the computer when trying out different candidate values for step size *k*. However, in this article, the parameters of the objective function P_w are unknown and vary as the Rx coils move. Trying out different candidate values for step size *k* is needed to change

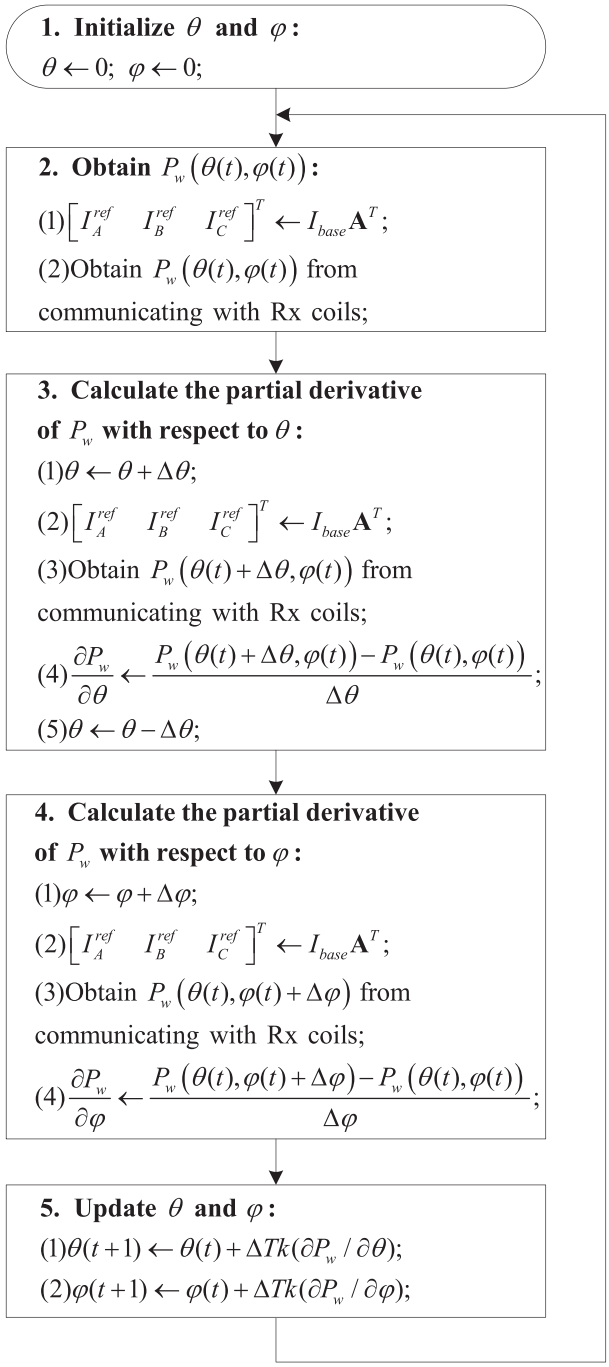

Fig. 5. Diagram block of the proposed algorithm.

θ and φ, to regulate the Tx coil current, and communicate with Rx coils to obtain the value of P_w. In this situation, the power transfer will fluctuate. Hence, the line search methods cannot be adopted here. In this article, the value of the step size *k* is simply set as a fixed positive number, which is obtained by trial and error in the experiment.

As shown in Fig. 5, the proposed algorithm is divided into five parts. In the first part, θ and φ are initialized to zero. In the second part, $P_w(\theta(t), \varphi(t))$ is obtained from communicating with Rx coils. In the third and fourth parts, the gradients of P_w are calculated. Specifically, $\partial P_w/\partial\theta$ and $\partial P_w/\partial\varphi$ are calculated in the third and fourth part, respectively. Finally, in the fifth part, θ

and φ are updated based on the calculated gradients. The loop between the second part and the fifth part will run once at each period of ΔT.

B. Proof of the Correctness and Convergence of the Algorithm

To guarantee the correctness and convergence of the proposed algorithm, the following theorem needs to be proved.

Theorem 1: If $\theta(t)$ and $\varphi(t)$ evolve based on (13), every point starting from $\mathbb{D}$ converges to $\mathbb{N}$ as $t \to \infty$, where

$$\mathbb{D} = \{\theta, \varphi | \theta \in [0, \pi], \varphi \in [0, 2\pi)\}$$

$$\mathbb{N} = \left\{(\theta, \varphi) \in \mathbb{D} | \mathbf{A}^T = \mathbf{Q_1}\right\}.$$

Proof of Theorem 1: A Lyapunov function candidate is $V(\theta, \varphi) = -P_w(\theta, \varphi)$. Considering (13), $\dot{V}(\theta, \varphi) = -k((\partial P_w/\partial\theta)^2 + (\partial P_w/\partial\varphi)^2)$. $\dot{V}(\theta, \varphi)$ is negative semidefinite. Let $\mathbb{E}$ represent the set when $\dot{V}(\theta, \varphi) = 0$ as $\mathbb{E} = \{(\theta, \varphi) \in \mathbb{D} | \dot{V}(\theta, \varphi) = 0\}$. Let $\mathbb{F}$ be the largest invariant set in $\mathbb{E}$. According to the LaSalle's invariance principle [23], every point starting in $\mathbb{D}$ approaches $\mathbb{F}$ as $t \to \infty$. It needs to prove that $\mathbb{F} \subset \mathbb{N}$. $\mathbb{E}$ can be a collection of $\mathbb{E}_j$ as $\mathbb{E} = \{\mathbb{E}_j\}$, where $\mathbb{E}_j = \{(\theta, \varphi) \in \mathbb{D} | \mathbf{A}^T = \mathbf{Q}_j\}$ and j equals 1, 2, or 3. Especially, $\mathbb{E}_1 = \mathbb{N}$. Let $\mathbf{B}_j$ be the Jacobian matrix of (13) at $(\theta, \varphi) \in \mathbb{E}_j$ as

$$\mathbf{B}_j = k \left[\begin{array}{cc} \partial {P_w}^2(\theta, \varphi)/\partial\theta^2 & \partial {P_w}^2(\theta, \varphi)/\partial\theta\partial\varphi \\ \partial {P_w}^2(\theta, \varphi)/\partial\varphi\partial\theta & \partial {P_w}^2(\theta, \varphi)/\partial\varphi^2 \end{array} \right]\Bigg|_{(\theta,\varphi)\in\mathbb{E}_j}. \tag{19}$$

The set $\mathbb{E}_j$ is an invariant set if $\mathbf{B}_j$ is Hurwitz. The Jacobian matrixes $\mathbf{B}_j$ are

$$\mathbf{B}_1 = k \left[\begin{array}{cc} \rho_{2\alpha}^2\lambda_2 + \rho_{3\alpha}^2\lambda_3 - \lambda_1 & \rho_{2\alpha}\rho_{2\beta}\lambda_2 + \rho_{3\alpha}\rho_{3\beta}\lambda_3 \\ \rho_{2\alpha}\rho_{2\beta}\lambda_2 + \rho_{3\alpha}\rho_{3\beta}\lambda_3 & \rho_{2\beta}^2\lambda_2 + \rho_{3\beta}^2\lambda_3 - \sin^2\theta\lambda_1 \end{array} \right] \tag{20}$$

$$\mathbf{B}_2 = k \left[\begin{array}{cc} \rho_{1\alpha}^2\lambda_1 + \rho_{3\alpha}^2\lambda_3 - \lambda_2 & \rho_{1\alpha}\rho_{1\beta}\lambda_1 + \rho_{3\alpha}\rho_{3\beta}\lambda_3 \\ \rho_{1\alpha}\rho_{1\beta}\lambda_1 + \rho_{3\alpha}\rho_{3\beta}\lambda_3 & \rho_{1\beta}^2\lambda_1 + \rho_{3\beta}^2\lambda_3 - \sin^2\theta\lambda_2 \end{array} \right] \tag{21}$$

$$\mathbf{B}_3 = k \left[\begin{array}{cc} \rho_{2\alpha}^2\lambda_2 + \rho_{1\alpha}^2\lambda_1 - \lambda_3 & \rho_{2\alpha}\rho_{2\beta}\lambda_2 + \rho_{1\alpha}\rho_{1\beta}\lambda_1 \\ \rho_{2\alpha}\rho_{2\beta}\lambda_2 + \rho_{1\alpha}\rho_{1\beta}\lambda_1 & \rho_{2\beta}^2\lambda_2 + \rho_{1\beta}^2\lambda_1 - \sin^2\theta\lambda_3 \end{array} \right] \tag{22}$$

where $\rho_{j\alpha} = \boldsymbol{\alpha} \cdot \mathbf{Q}_j$ and $\rho_{j\beta} = \boldsymbol{\beta} \cdot \mathbf{Q}_j$. $\boldsymbol{\alpha} = \partial\mathbf{A}^T/\partial\theta$ and $\boldsymbol{\beta} = \partial\mathbf{A}^T/\partial\varphi$. Their eigenfunction is obtained as

$$\det(\lambda\mathbf{I} - \mathbf{B}_j) = \lambda^2 + a_j\lambda + b_j \tag{23}$$

where

$$a_1 = \lambda_1 - \rho_{2\alpha}^2\lambda_2 - \rho_{3\alpha}^2\lambda_3 + \sin\theta^2\lambda_1 - \rho_{2\beta}^2\lambda_2 - \rho_{3\beta}^2\lambda_3$$

$$a_2 = \lambda_2 - \rho_{1\alpha}^2\lambda_1 - \rho_{3\alpha}^2\lambda_3 + \sin\theta^2\lambda_2 - \rho_{1\beta}^2\,\lambda_1 - \rho_{3\beta}^2\lambda_3$$

$$a_3 = \lambda_3 - \rho_{2\alpha}^2\lambda_2 - \rho_{1\alpha}^2\lambda_1 + \sin\theta^2\lambda_3 - \rho_{2\beta}^2\lambda_2 - \rho_{1\beta}^2\lambda_1$$

$$b_1 = \sin\theta^2(\lambda_1 - \lambda_3)(\lambda_1 - \lambda_2) \quad b_2 = \sin\theta^2(\lambda_2 - \lambda_3)(\lambda_2 - \lambda_1)$$

$$b_3 = \sin\theta^2(\lambda_3 - \lambda_2)(\lambda_3 - \lambda_1) \quad \mathbf{I} = \mathrm{diag}(1, 1).$$

$a_1 > 0$ and $b_1 > 0$, $\mathbf{B}_1$ is Hurwitz. However, $a_3 < 0$ and $b_2 < 0$. $\mathbf{B}_2$ and $\mathbf{B}_3$ are not Hurwitz. $\mathbb{E}_1$ is the largest invariant set in $\mathbb{E}$. In general, $\mathbb{F} = \mathbb{N} = \mathbb{E}_1$, and thus, the proof of Theorem 1 is completed. ■

C. Frequency Splitting Problem

This article only focuses on regulating the current amplitude and phase of the three Tx coils at a fixed operation frequency. At that frequency, the maximum power point is tracked. However, the power transfer could decay if the operation frequency is inappropriate.

It is reported that frequency splitting could occur when there is a strong coupling between Tx and Rx coils [24], or different Rx coils [25]. In this situation, to maintain the power transfer efficiency, fixing the frequency is inappropriate. The methods that are used to handle the frequency splitting problem can be divided into two kinds.

1) The operation frequency is changeable and controlled to track the splitting frequency [24]–[26], to maintain the power transfer efficiency.
2) The coils and the compensation circuits are carefully designed, so that the system has only one constant resonance frequency [27], [28] and the frequency splitting phenomenon is avoided.

Since the operation frequency is not controlled in the proposed algorithm, it cannot handle the frequency splitting problem by itself. However, it can work together with those methods that are used to handle the frequency splitting problem. The proposed algorithm can work with these methods in the forms as follows.

1) As for the first kind of methods, the frequency control method is first run to determine the operation frequency. Then, the proposed algorithm is run to regulate the amplitude and phase of the Tx coil current at the previously determined frequency to maximize the power transfer. Repeating these two steps again and again can handle the frequency splitting problem and maximize the power transfer.
2) As for the second kind of methods, the proposed algorithm only needs to be run at that constant resonance frequency.

Then, the frequency splitting problem is handled with the help of those methods.

VI. Experimental Verification of the Proposed Algorithm

A 3-D WPT system prototype, with triple orthogonal Tx coils and multiple single Rx coil configuration, is built up to verify the proposed algorithm. Without loss of generality, two Rx coils are used to represent multiple mobile Rx coils.

Fig. 6 shows the schematic block diagram of the 3-D WPT system prototype. Points $\mathbf{O}$, $\mathbf{P}_1$, and $\mathbf{P}_2$ represent centers of the Tx coils, first and second Rx coil, respectively. Point $\mathbf{O}$'s coordinate is set to be (0,0,0). Fig. 7 shows the 3-D WPT system prototype test rig in the top viewport. The Tx coils A, B, and C are marked in blue, red, and green, respectively. In this experiment, the circular coils, as those commonly used in the commercial devices supporting wireless charging, are chosen as Rx coils to

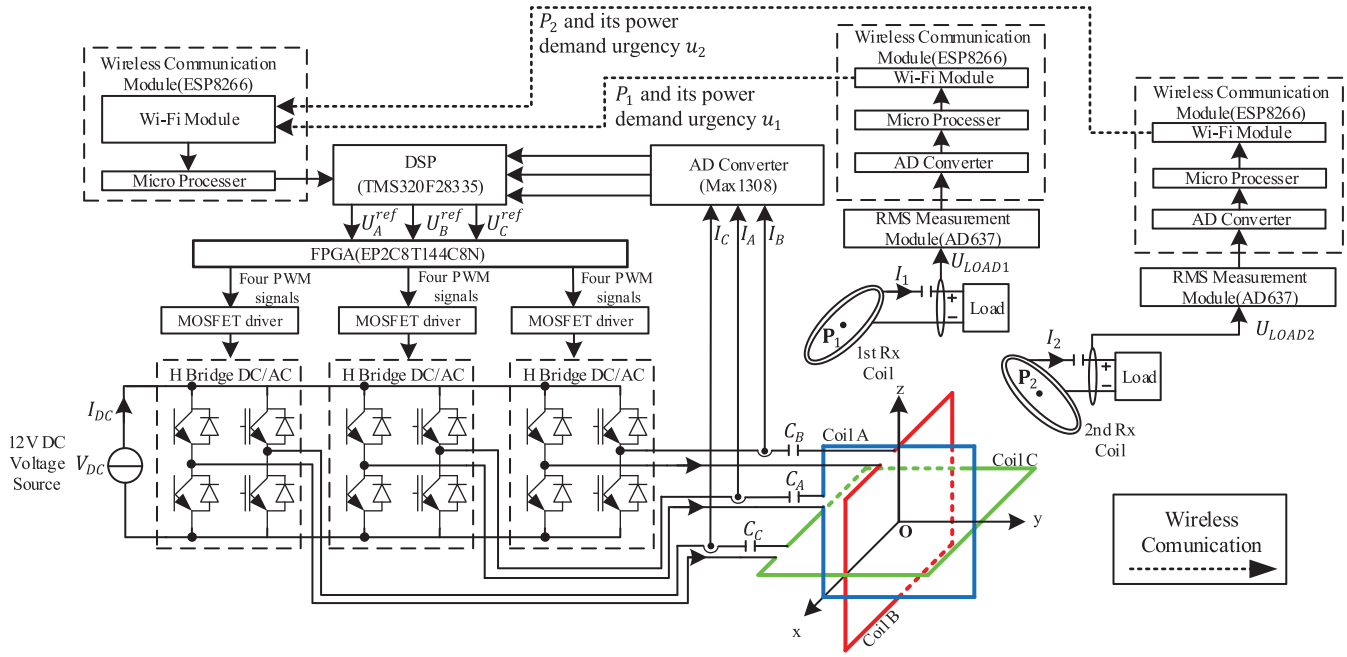

Fig. 6. Schematic block diagram of the 3-D field orientation WPT system experimental setup.

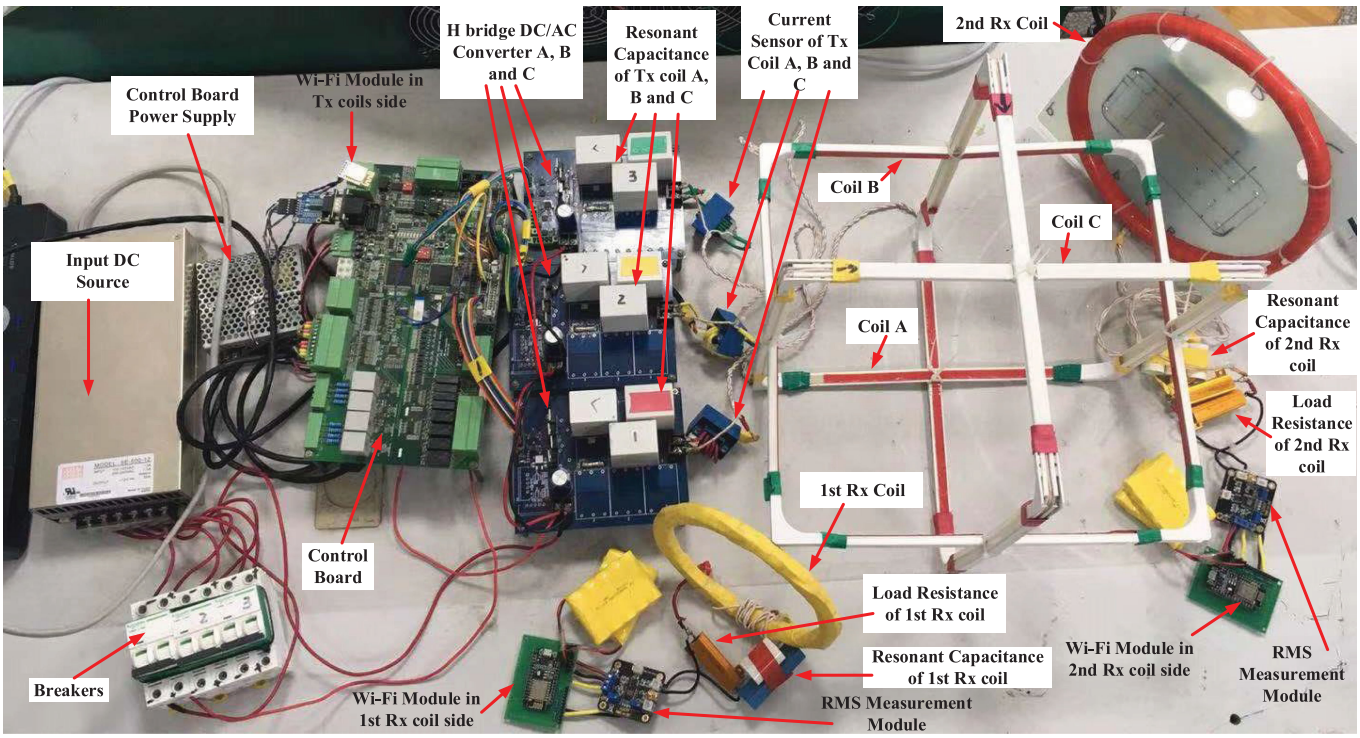

Fig. 7. Test rig of the 3-D WPT system experimental setup.

simulate commercial devices. As for the Tx coils, square coils are chosen as they can be easily fixed on the table directly for convenience. Circular coils need extra materials to be fixed on the table. Actually, designing the most suitable coil shape is an important problem, but it is outside the scope of this article. The proposed algorithm can maximize the power transfer regardless of the coils' shape. The coils' shape used in this experiment is not optimal, but it can still be used to verify the proposed algorithm.

I_A, I_B, and I_C are sampled by three independent current transducers HAS 50-S (LEM). A digital signal processor (DSP, TMS32028335) is used to get the value of I_A, I_B, and I_C, and to regulate them to the reference values by feedback control.

TABLE II
ACTUAL COIL PARAMETERS OF THE 3-D WPT SYSTEM

Symbol	Length of side (mm)	Turns	Wire radius (mm)
Tx Coil A	328	3	2.2
Tx Coil B	328	3	2.2
Tx Coil C	328	3	2.2
First Rx coil	150	30	2.2
Second Rx coil	276	15	2.2

TABLE III
ACTUAL PARAMETERS OF THE 3-D WPT SYSTEM

Symbol	Value	Symbol	Value	Symbol	Value
L_A	10.06 μH	C_A	6.61 μF	R_A	50.23 mΩ
L_B	10.09 μH	C_B	6.59 μF	R_B	50.30 mΩ
L_C	10.11 μH	C_C	6.58 μF	R_C	50.43 mΩ
L_1	101.28 μH	C_1	0.66 μF	R_1	1.6 Ω
L_2	245.51 μH	C_2	0.27 μF	R_2	0.8 Ω

Then, the proposed algorithm, listed in Fig. 5, is run in the DSP. The DSP sent the values of the required U_A, U_B, and U_C to a field-programmable gate array (FPGA EP2C8J144C8N). The FPGA generates the metal oxide semiconductor field effect transistor (MOSFET) drive signal to control the three H-bridge dc/ac converters. Then, the desired U_A, U_B, and U_C are generated by the H bridge dc/ac converter. All the three H-bridge dc/ac converters are powered by a 12-V dc voltage source. The power transfer to the two Rx coils and their power demand urgencies are wirelessly communicated into the control system. The wireless communication is realized by Wi-Fi technologies. A Wi-Fi module, ESP8266, is embedded into the Tx coil side, which works in the hotspot mode. It is also embedded into each Rx coil side, which works in station mode. Besides the Wi-Fi module, ESP8266 is also integrated with a 32-bit Tensilica processor and an analog-to-digital (A/D) converter. The load resistance voltage U_{LOAD1} or U_{LOAD2} is converted to its root-mean-square (rms) value by an rms measurement module (AD637). The analog rms value is converted to a digital signal by the A/D converter. Then, the processor calculates the power transfer to the Rx coil and decides its power demand urgency. The Wi-Fi module embedded in each Rx coil side communicates the power transfer and its power demand urgency to the Wi-Fi module embedded in the Tx coil side wirelessly.

The voltage and current frequency of the Tx coils are controlled in 20 kHz. The control loop time ΔT is designed to be 10 ms. Table II shows the actual coil parameters of the 3-D WPT system. Table III shows the parameters of the 3-D WPT system. The parameters of the proposed algorithm in Section V are listed in Table IV.

In order to verify that the proposed algorithm can adapt to the power demand variations and movement of the devices, the experiments are conducted under two application scenarios.

TABLE IV
PARAMETERS OF THE PROPOSED ALGORITHM

Symbol	Value	Symbol	Value
I_{base}	8 A	k	0.02
$\Delta\theta$	0.1 rad	$\Delta\varphi$	0.1 rad

1) Scenario A, in which the two Rx coils stay still at arbitrary space with an arbitrary orientation, and the power demand variation is realized by changing the two power allocation weights w_1 and w_2. In practice, the power demand urgency u_n of every device is sent to the WPT system via wireless communication, and the WPT gives every device a power allocation weight according to (5). In this experiment, the WPT system directly changes the power allocation weights for simplicity. The two currents I_1 and I_2 are observed to represent the power transfer and show whether they converge to the optimal solutions of (10) before and after the weights w_1 and w_2 change. Meanwhile, the convergence time after the weights w_1 and w_2 change is also tested to show the dynamic performance of the proposed algorithm.
2) Scenario B, in which one of the Rx coils moves from one arbitrary space with arbitrary orientation to another. The two Rx coil currents are observed to represent the power transfer and show whether they converge to the optimal solutions of (10) before the Rx coil starts moving and after it stops moving. Since the Rx coils cannot be moved instantly, the convergence time is not tested in this situation.

Besides the proposed algorithm, a traversal search algorithm is also developed and used to check whether the maximum power transfer is achieved. The traversal search algorithm tests every θ and φ in the solution space $\mathbb{D}$ repeatedly. The block diagram of the traversal search algorithm is shown in Appendix II. If the power transfer when running the proposed algorithm is larger than that at any moment when running the traversal search algorithm, the maximum power transfer is achieved.

Since the proposed algorithm is independent of the positions and orientations of the Rx coils, the positions and orientations are arbitrary in the following experiment. However, to make the experimental results more complete, the specific positions and orientations of the Rx coils are listed. The positions are represented by the coordinate of $\mathbf{P}_1$ and $\mathbf{P}_2$. The orientations are represented by rotating from the initial orientation, which is the direction of z-axis. The rotation is represented by the quaternion, which is more compact than rotation matrices.

A. Power Transfer to Rx Coils in Arbitrary Positions With Arbitrary Orientations When Their Power Demands Vary

The proposed algorithm can work regardless of the positions and orientations of the Rx coils. In this experiment, the Rx coils are placed in arbitrary positions with arbitrary orientations.

The position of the first Rx coil is $\mathbf{P}_1$ $(-7.0, -10.0, 10.0)$ cm. The distance between the center of the Tx coils and the first Rx coil is 15.8 cm. The position of second Rx coil is $\mathbf{P}_2$

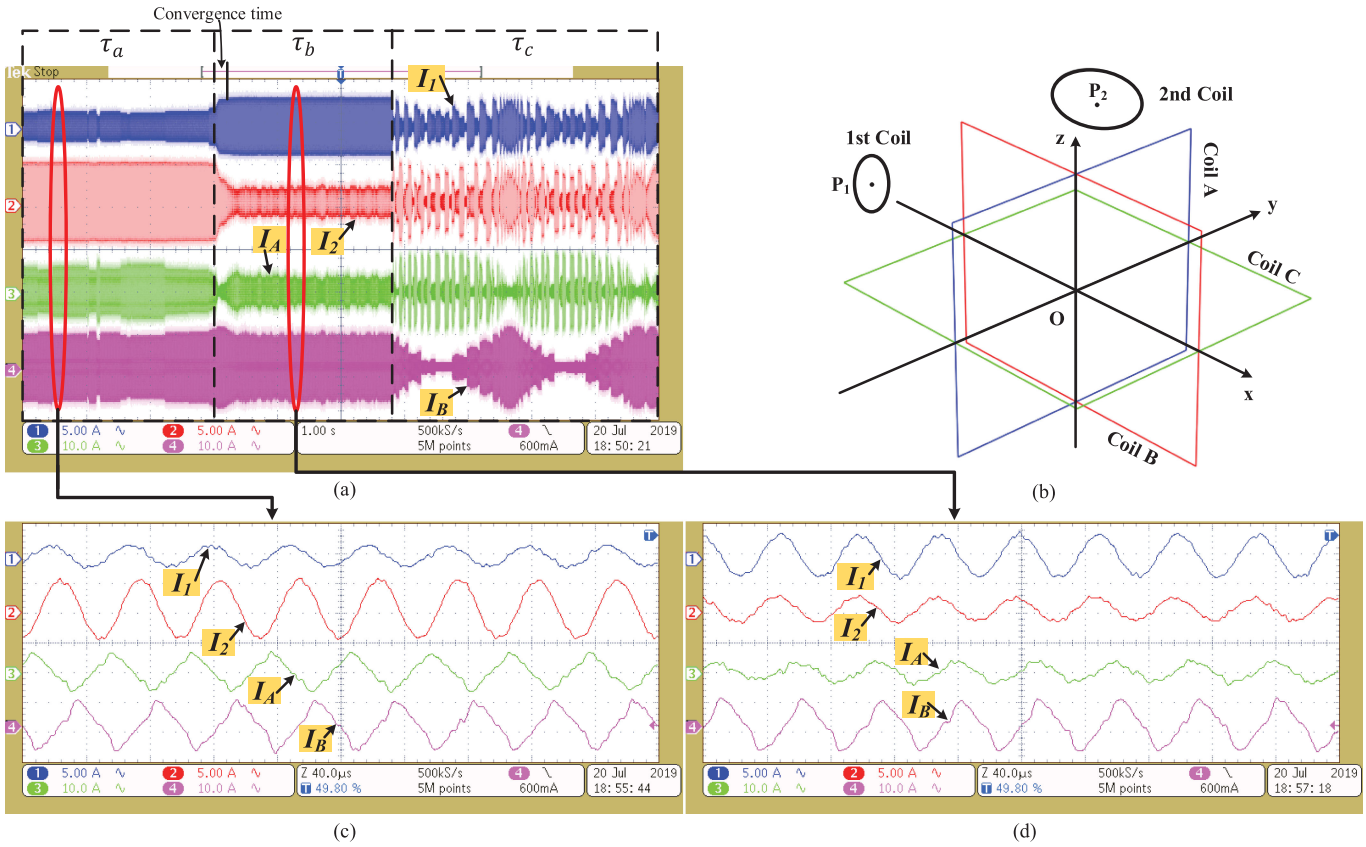

Fig. 8. Experimental results for maximum power transfer when the Rx coils are in arbitrary positions with arbitrary orientations. (a) Overview waveform. (b) Specific positions and orientations of the first and second Rx coils in this experiment. (c) Detailed waveform in the time interval τ_a. (d) Detailed waveform in the time interval τ_b.

$(-12.0, 14.0, 6.0)$ cm. The distance between the center of the Tx coils and the second Rx coil is 19.4 cm. The orientation of the first Rx coil, which is represented by the quaternion, is $0.57-0.81\mathbf{i}+0.02\mathbf{j}-0.14\mathbf{k}$. The orientation of the second Rx coil is $0.67-0.32\mathbf{i}-0.57\mathbf{j}-0.35\mathbf{k}$.

Fig. 8 shows the experimental results for power transfer to the Rx coils. The overview waveforms are shown in Fig. 8(a). The positions, orientations, and movement of the first and second Rx coils are shown in Fig. 8(b). The detailed waveforms in the time interval τ_b are shown in Fig. 8(c), and the detailed waveforms in the time interval τ_d are shown in Fig. 8(d).

During the time interval τ_a, w_1 and w_2 are set to be 0 and 1 to give the most priority to the second Rx coil. During the time interval τ_b, w_1 and w_2 are set to be 1 and 0 to give the most priority to the first Rx coil. Then, the second Rx coil will obtain as much power as possible during the time interval τ_a and the first Rx coil will obtain as much power as possible during the time interval τ_b. During the time interval τ_c, the traversal search algorithm is run to verify the proposed algorithm. It can be seen in Fig. 8 that, during the time interval τ_b, after the proposed algorithm converges, the power transfer to the first Rx coil is larger than that any moment in τ_c. The power transfer to the second Rx coil during τ_a is also larger than that at any moment in the time interval τ_c. Hence, the first and second Rx coils indeed obtain as much power as possible in τ_a and τ_b, respectively. It means that the proposed algorithm can adapt to the power demand variation.

It can also be seen in Fig. 8 that it needs 0.2 s to converge when the weights change. The relationship between the weight w_n and the power demand urgency u_n is (5). Hence, in this experiment, the weight change is used to simulate the power demand urgency change for simplicity. The convergence time is compared with the speed of change of power demand urgencies. In practice, the power demand urgencies of multiple devices will not change quickly. Hence, comparing to the speed of change of the power demand urgencies, the convergence time of the proposed algorithm is fast enough.

B. Power Transfer to Rx Coils When They Are Moving From One Arbitrary Position With Arbitrary Orientation to Another

Figs. 9 and 10 show the experimental results for power transfer to Rx coils when they are moving. During the time interval τ_a, the traversal search algorithm is run. Then, during the time interval τ_b, τ_c, and τ_d, the proposed algorithm is run. At last, during the time interval τ_e, the traversal search algorithm is run again. The second Rx coil is moving during the time interval τ_c in Fig. 9, while the first Rx coil is moving during the time interval τ_c in Fig. 10. The movements are arbitrary.w_1 and w_2 are set to be 1 and 0 to give the most priority to the first Rx coil.

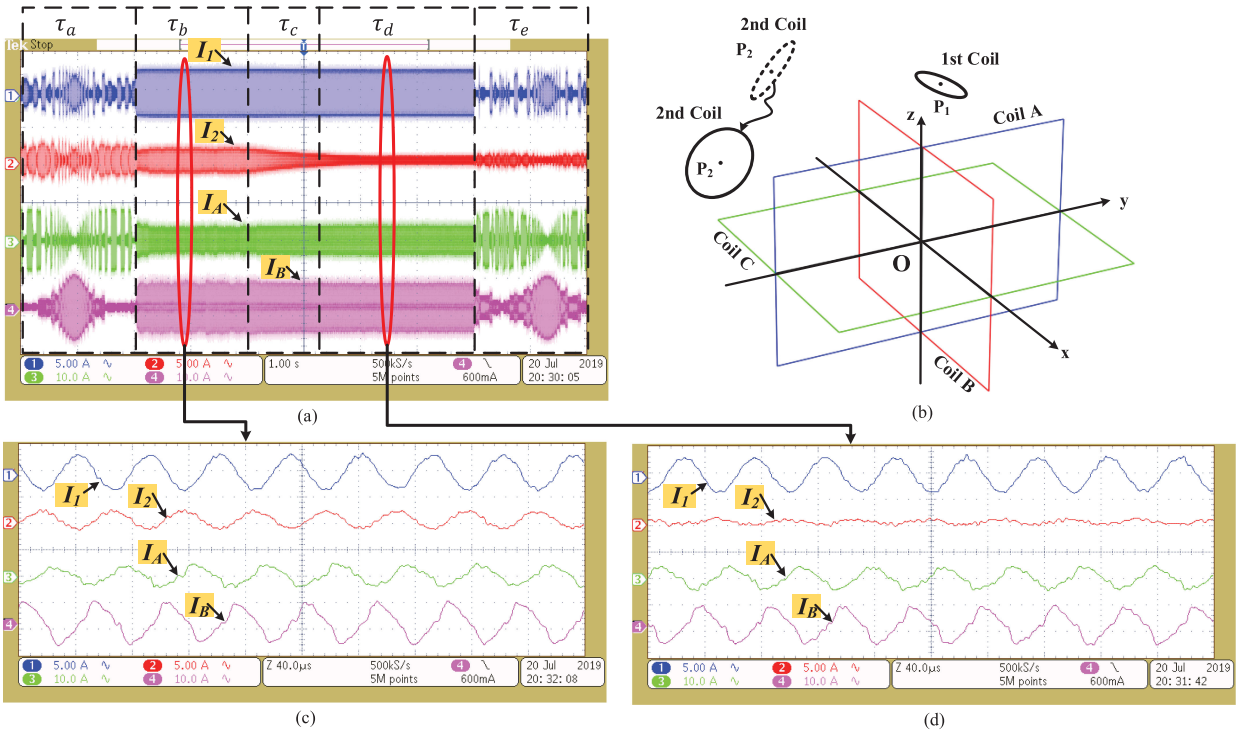

Fig. 9. Experimental results for maximum power transfer to first Rx coil when the second Rx coil is moving. (a) Overview waveform. (b) Specific positions, orientations, and movement of the first and second Rx coils in this experiment. (c) Detailed waveform in the time interval τ_b. (d) Detailed waveform in the time interval τ_d.

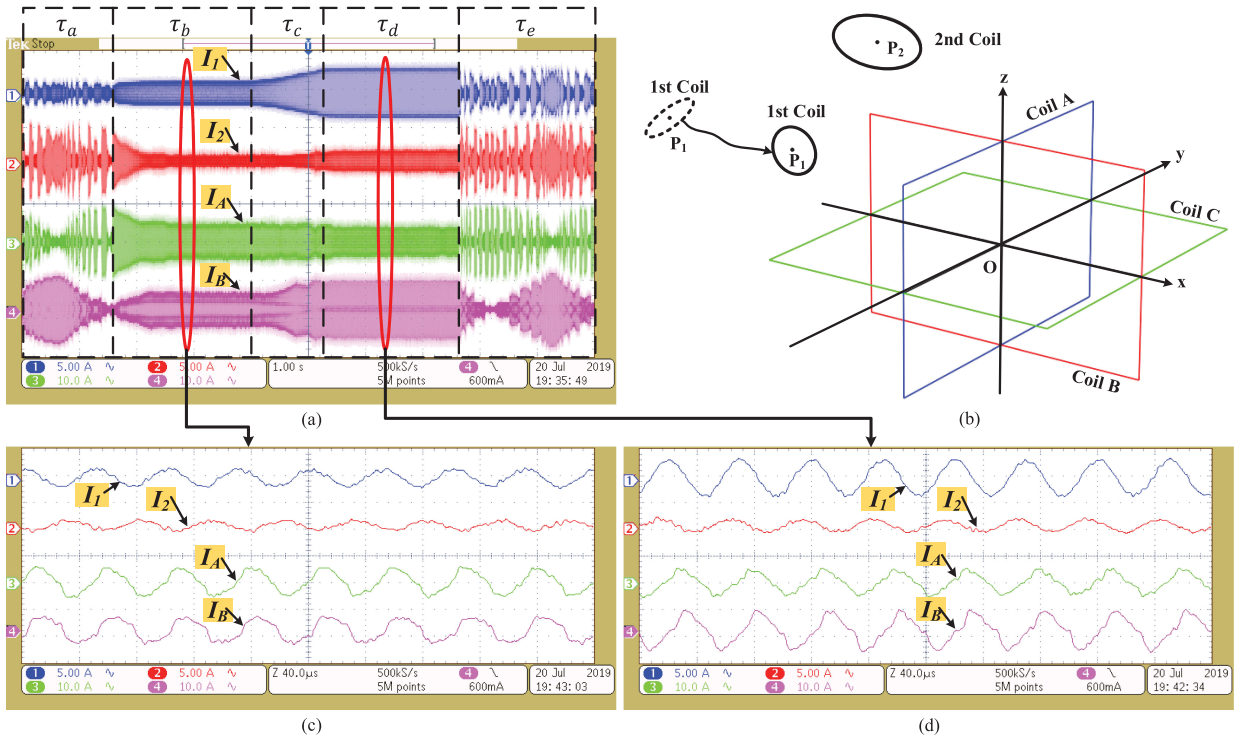

Fig. 10. Experimental results for maximum power transfer to the first Rx coil when the first Rx coil is moving. (a) Overview waveform. (b) Specific positions, orientations, and movement of the first and second Rx coils in this experiment. (c) Detailed waveform in the time interval τ_b. (d) Detailed waveform in the time interval τ_d.

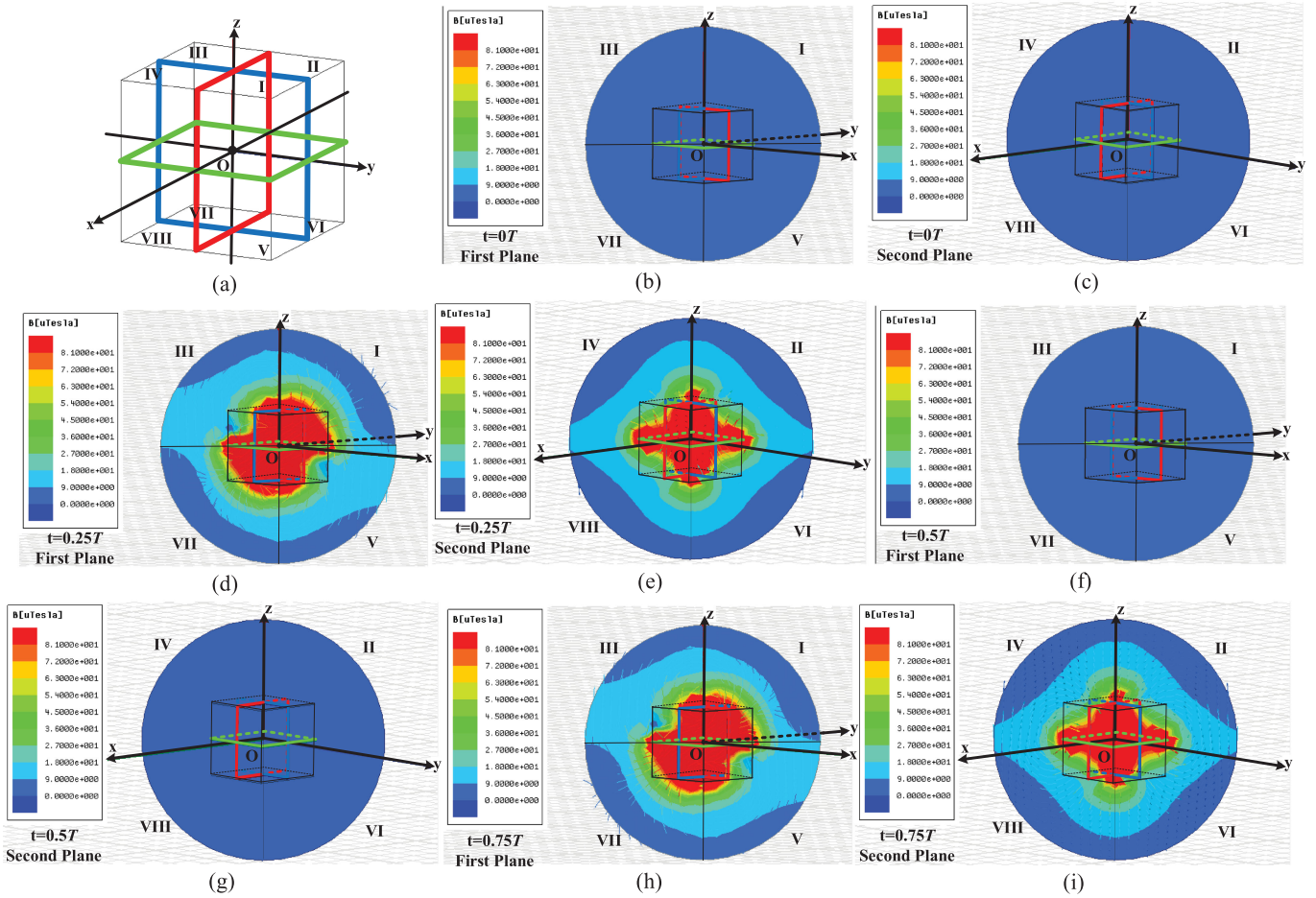

Fig. 11. Simulation results for EMI analysis of the triple orthogonal Tx coil current control principle when both θ and φ in (1) are set to be $\pi/4$. (a) Eight quadrants of the 3-D coordinate system. Magnetic field intensity on (b) first plane when $t = 0T$, (c) second plane when $t = 0T$, (d) first plane when $t = 0.25T$, (e) second plane when $t = 0.25T$, (f) first plane when $t = 0.5T$, (g) second plane when $t = 0.5T$, (h) first plane when $t = 0.75T$, and (i) second plane when $t = 0.75T$.

In Fig. 9, the position of the first Rx coil is $\mathbf{P}_1$ (-10.0, 6.0, 10.0) cm. The distance between the center of the Tx coils and the first Rx coil is 15.4 cm. The orientation of the first Rx coil, which is represented by the quaternion, is $0.48{+}0.85\mathbf{i}{+}0.20\mathbf{j}{-}0.11\mathbf{k}$. The initial position of the second Rx coil is $\mathbf{P}_2$ (-15.0, -4.0, 12.0) cm. The distance between the center of the Tx coils and the second Rx coil is 19.6 cm. The initial orientation of the second Rx coil is $0.22{+}0.31\mathbf{i}{+}0.75\mathbf{j}{+}0.54\mathbf{k}$. The final position of the second Rx coil is $\mathbf{P}_2$ (-4.0, -12.0, 10.0) cm. The distance between the center of the Tx coils and the second Rx coil is 16.1 cm. The final orientation of the second Rx coil is $0.20{-}0.37\mathbf{i}{-}0.69\mathbf{j}{-}0.59\mathbf{k}$.

In Fig. 10, the initial position of the first Rx coil is $\mathbf{P}_1$ (-14.0, -14.0, 14.0) cm. The distance between the center of the Tx coils and the first Rx coil is 24.2 cm. The initial orientation of the first Rx coil is $0.85{+}0.51\mathbf{i}{-}0.35\mathbf{j}{-}0.35\mathbf{k}$. The final position of the first Rx coil is $\mathbf{P}_1$ (-8.0, -10.0, 11.0) cm. The distance between the center of the Tx coils and the first Rx coil is 16.9 cm. The final orientation of the first Rx coil is $0.76{+}0.65\mathbf{i}{-}0.08\mathbf{j}{-}0.09\mathbf{k}$. The position of the second Rx coil is $\mathbf{P}_2$ (-14.0, 6.0, 14.0) cm. The distance between the center of the Tx coils and the second Rx coil is 20.7 cm. The orientation of the second Rx coil is $0.59{+}0.78\mathbf{i}{-}0.04\mathbf{j}{+}0.21\mathbf{k}$.

The overview waveforms are shown in Figs. 9(a) and 10(a). The positions, orientations, and movement of the first and second Rx coils are shown in Figs. 9(b) and 10(b). The detailed waveforms in the time interval τ_b are shown in Figs. 9(c) and 10(c). The detailed waveforms in the time interval τ_d are shown in Figs. 9(d) and 10(d).

The movement will change the mutual inductances between the coils. In Fig. 9, the mutual inductance M_{A2}, M_{B2}, M_{C2}, and M_{12} will change as the second Rx coil moves. Since M_{A2}, M_{B2}, and M_{C2} changes, the current and power transfer to the second Rx coil obviously become smaller. The current and power transfer to the first Rx coil also change slightly due to these variations of mutual inductance M_{12}. In Fig. 10, although the WPT system still transfers maximum power to the first Rx coil, the power transfer ability to the first Rx coil changes as the position and orientation of the first Rx coil change. It can be seen that the current of the first Rx coil becomes larger obviously due to the variations of M_{A1}, M_{B1}, and M_{C1}. The current and power transfer to the second

Rx coil also change slightly due to these variations of mutual inductance M_{12}.

Although the current and power transfer to the first Rx coil change in both two situations, the power transfer to it during τ_b after the proposed algorithm converges is larger than that at any moment during τ_a. The power transfer to it during τ_d is also larger than that at any moment during τ_e. The optimal solutions of (10) have still been obtained regardless of the movement of the Rx coils. It means that the proposed algorithm can adapt to the Rx coils' movement.

C. EMI Analysis of the Triple Orthogonal Tx Coil Current Control Principle

In this section, the simulation results of the EMI analysis of the triple orthogonal Tx coil current control principle are presented. According to (2), the magnetic field direction can be shaped by the current control principle (1). The specific direction is represented by θ and φ, which are the polar and azimuthal angle in the spherical coordinate. Then, the magnetic field in other directions will decrease relatively. By the proposed algorithm, the specific direction usually converges to the place of the target devices so that the power transfer can be maximized. As a result, EMI on other devices will be reduced.

Fig. 11 shows the simulation results of the magnetic field. The three orthogonal Tx coils are excited by three independent current sources. The theoretical magnetic field is simulated in the software "Ansys Maxwell." Both θ and φ in (1) are set to be $\pi/4$. T represents the time period, which is 50 μs. The 3-D coordinate system is divided into eight quadrants as shown in Fig. 11(a). Magnetic field intensity on two planes is shown in Fig. 11(b)–(i). The z-axis is on both the two planes. The center of the two planes is the original point **O** of the 3-D coordinate system. The angles between the first plane and the x- and y-axes are $\pi/4$ and $7\pi/4$, respectively. Then, the magnetic field intensity in quadrants I, III, V, and VII can be shown in the first plane. The angles between the second plane and the x- and y- axes are $7\pi/4$ and $\pi/4$, respectively. Then, the magnetic field intensity in quadrants II, IV, VI, and VIII can be shown in the second plane. In Fig. 11(b)–(i), the time is set to be $0T$, $0.25T$, $0.5T$, and $0.75T$.

From the simulation results, it could be seen that the magnetic field intensity in quadrants I and VI is enhanced, while it is weakened in the other quadrants. Hence, these simulation results verify that using the current control principle and the proposed algorithm can reduce EMI on other devices.

VII. Conclusion

In this article, an algorithm has been proposed to achieve simultaneous power transfer to multiple moving Rx coils with different power demands in 3-D space. An objective function with respect to the amplitude and phase differences of the Tx coil currents has been formulated through using a weighted sum of the power transfer to multiple moving devices. The algorithm has been developed using the gradient ascent method to optimize the objective function, and its correctness and convergence have been proved based on LaSalle's invariance principle.

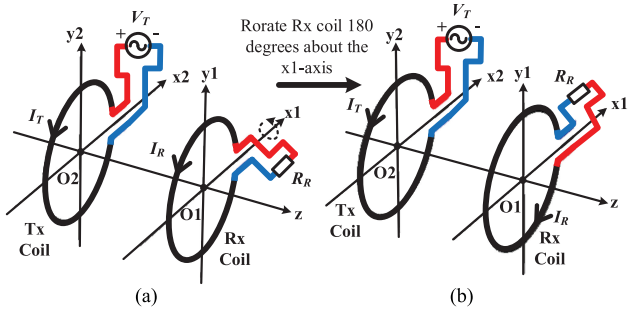

Fig. 12. Situation when the Rx coil is with different orientations.

The proposed algorithm does not need to know the positions and orientations of the multiple moving devices, which is difficult to obtain in practice. The experimental results have shown that the proposed algorithm can adapt to the movement and power demand variation of the devices. The convergence time of the proposed algorithm is 0.2 s after the devices' power demand urgencies change. The proposed algorithm may have a great application prospect in the field of 3-D wireless charging of multiple moving devices.

Appendix I

Fig. 12 shows the situation when the Rx coil has different orientations. Two same circular coils are used to represent Tx and Rx coils. The Tx and Rx coils are parallel to each other and perpendicular to the z-axis. Their coil centers are on the z-axis. The circuit in the left side of Fig. 12 is the original circuit, while the circuit in the right side of Fig. 12 is obtained by rotating the Rx coil 180° about the $x1$-axis. The mutual inductance between the Tx and Rx coils is denoted as M. The self-inductances of the Tx and Rx coils are denoted as L_T and L_R, respectively. The currents of the Tx and Rx coils are denoted as I_T and I_R, respectively. The Tx coil is series connected with an ac power source V_T, while the Rx coil is series connected with a resistor R_R. The coil resistances are neglected.

Commonly, the mutual inductance is a positive variable and M will not change after the rotation shown in Fig. 12. Let us assume that M is equal to 10 mH. Then, two different equations are needed to represent the mathematical model of the circuits in the left and right sides. The mathematic model of the circuit in the left side of Fig. 12 is

$$\begin{bmatrix} j\omega L_T & j\omega M \\ j\omega M & R_R + j\omega L_R \end{bmatrix} \begin{bmatrix} I_T \\ I_R \end{bmatrix} = \begin{bmatrix} V_T \\ 0 \end{bmatrix}. \tag{24}$$

The mathematical model of the circuit in the right side of Fig. 12 is

$$\begin{bmatrix} j\omega L_T & -j\omega M \\ -j\omega M & R_R + j\omega L_R \end{bmatrix} \begin{bmatrix} I_T \\ I_R \end{bmatrix} = \begin{bmatrix} V_T \\ 0 \end{bmatrix}. \tag{25}$$

However, if the meaning of mutual inductance is generalized, it could be a positive or negative variable. Then, M is equal to 10 mH in the original circuit, while it will be equal to -10 mH after the rotation shown in Fig. 12. Hence, only one uniform

equation can represent the mathematical model of these two circuits. The equation is

$$\begin{bmatrix} j\omega L_T & j\omega M \\ j\omega M & R_R + j\omega L_R \end{bmatrix} \begin{bmatrix} I_T \\ I_R \end{bmatrix} = \begin{bmatrix} V_T \\ 0 \end{bmatrix}. \quad (26)$$

APPENDIX II

The block diagram of the traversal search algorithm is shown as follows.

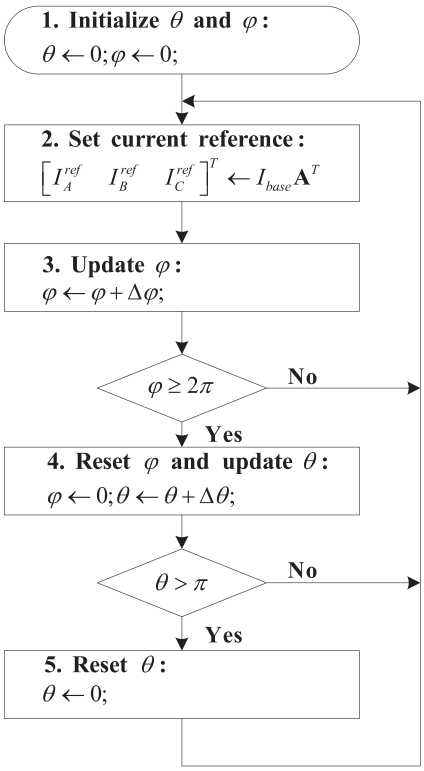

Fig. 13. Block diagram of the traversal search algorithm.

REFERENCE

[1] G. A. Covic and J. T. Boys, "Inductive power transfer," *Proc. IEEE*, vol. 101, no. 6, pp. 1276–1289, Jun. 2013.

[2] J. S. Choi, E. S. Lee, B. G. Choi, S. H. Han, and C. T. Rim, "Six degrees of freedom wide-range IPT for multiple IoT by DQ rotating magnetic field," in *Proc. IEEE Appl. Power Electron. Conf. Expo.*, 2017, pp. 3730–3737.

[3] E. S. Lee, J. S. Choi, H. S. Son, S. H. Han, and C. T. Rim, "Six degrees of freedom wide-range ubiquitous IPT for IoT by DQ magnetic field," *IEEE Trans. Power Electron.*, vol. 32, no. 11, pp. 8258–8276, Nov. 2017.

[4] B. H. Choi, E. S. Lee, Y. H. Sohn, G. C. Jang, and C. T. Rim, "Six degrees of freedom mobile inductive power transfer by crossed dipole Tx and Rx coils," *IEEE Trans. Power Electron.*, vol. 31, no. 4, pp. 3252–3272, Apr. 2016.

[5] B. H. Choi, E. S. Lee, Y. H. Sohn, J. H. Kim, and C. T. Rim, "Crossed dipole coils for an omnidirectional wireless power zone with DQ rotating magnetic field," in *Proc. IEEE Energy Convers. Congr. Expo.*, Sep. 2015, pp. 2261–2268.

[6] Y. Lim, H. Ahn, and J. Park, "Analysis of antenna structure for energy beamforming in wireless power transfer," *IEEE Trans. Antennas Propag.*, vol. 65, no. 11, pp. 6085–6094, Nov. 2017.

[7] E. S. Lee, B. H. Choi, Y. H. Sohn, G. C. Lim, and C. T. Rim, "Multiple dipole receiving coils for 2-D omnidirectional wireless mobile charging under wireless power zone," in *Proc. IEEE Energy Convers. Congr. Expo.*, Sep. 2015, pp. 3209–3214.

[8] B. G. Choi, Y. H. Sohn, E. S. Lee, S. H. Han, H. R. Kim, and C. T. Rim, "Coreless transmitting coils with conductive magnetic shield for wide-range ubiquitous IPT," *IEEE Trans. Power Electron.*, vol. 34, no. 3, pp. 2539–2552, Mar. 2019.

[9] B. G. Choi, E. S. Lee, Y. H. Sohn, S. H. Han, H. R. Kim, and C. T. Rim, "Coreless transmitting coils with metal shield for wide-range ubiquitous IPT," in *Proc. IEEE 3rd Int. Future Energy Electron. Conf. ECCE Asia*, Jun. 2017, pp. 7–12.

[10] E. S. Lee, Y. H. Sohn, B. G. Choi, S. H. Han, and C. T. Rim, "A modularized IPT with magnetic shielding for a wide-range ubiquitous Wi-power zone," *IEEE Trans. Power Electron.*, vol. 33, no. 11, pp. 9669–9690, Nov. 2018.

[11] E. S. Lee, Y. H. Sohn, M. R. Sonapreetha, S. H. Han, and C. T. Rim, "Wide-range ubiquitous Wi-power zone by magnetic shielding," in *Proc. IEEE 3rd Int. Future Energy Electron. Conf. ECCE Asia*, Jul. 2017, pp. 13–18.

[12] P. Raval, D. Kacprzak, and A. P. Hu, "3D inductive power transfer power system," *Wireless Power Transfer*, vol. 1, pp. 51–64, Apr. 2014.

[13] P. Raval, D. Kacprzak, and A. P. Hu, "Multiphase inductive power transfer box based on a rotating magnetic field," *IEEE Trans. Ind. Electron.*, vol. 62, no. 2, pp. 795–802, Feb. 2015.

[14] P. Raval, D. Kacprzak, and A. P. Hu, "Analysis of flux leakage of a 3-D inductive power transfer system," *IEEE J. Emerg. Sel. Topics Power Electron.*, vol. 3, no. 1, pp. 205–214, Mar. 2015.

[15] Z. Zhang, B. Zhang, and J. Wang, "Optimal design of quadrature-shaped pickup for omnidirectional wireless power transfer," *IEEE Trans. Magn.*, vol. 54, no. 11, pp. 1–5, Nov. 2018.

[16] W. M. Ng, C. Zhang, D. Lin, and S. Y. R. Hui, "Two- and three-dimensional omnidirectional wireless power transfer," *IEEE Trans. Power Electron.*, vol. 29, no. 9, pp. 4470–4474, Sep. 2014.

[17] Y. Lim and J. Park, "A novel phase-control-based energy beamforming techniques in nonradiative wireless power transfer," *IEEE Trans. Power Electron.*, vol. 30, no. 11, pp. 6274–6287, Nov. 2015.

[18] C. Zhang, D. Lin, and S. Y. R. Hui, "Basic control principles of omnidirectional wireless power transfer," *IEEE Trans. Power Electron.*, vol. 31, no. 7, pp. 5215–5227, Jul. 2016.

[19] D. Lin, C. Zhang, and S. Y. R. Hui, "Mathematical analysis of omnidirectional wireless power transfer—Part-I: Two-dimensional systems," *IEEE Trans. Power Electron.*, vol. 32, no. 1, pp. 625–633, Jan. 2017.

[20] D. Lin, C. Zhang, and S. Y. R. Hui, "Mathematic analysis of omnidirectional wireless power transfer—Part-II Three-dimensional systems," *IEEE Trans. Power Electron.*, vol. 32, no. 1, pp. 613–624, Jan. 2017.

[21] Q. Zhu, M. Su, Y. Sun, W. Tang, and A. P. Hu, "Field orientation based on current amplitude and phase angle control for wireless power transfer," *IEEE Trans. Ind. Electron.*, vol. 65, no. 6, pp. 4758–4770, Jun. 2018.

[22] J. Nocedal and S. J. Wright, *Numerical Optimization*, 2nd ed. New York, NY, USA: Springer, 2006.

[23] H. K. Khalil, *Nonlinear Systems*, 3rd ed. Upper Saddle River, NJ, USA: Prentice-Hall, 2002.

[24] A. P. Sample, D. A. Meyer, and J. R. Smith, "Analysis, experimental results and range adaptation of magnetically coupled resonators for wireless power transfer," *IEEE Trans. Ind. Electron.*, vol. 58, no. 2, pp. 544–554, Feb. 2011.

[25] A. Bodrov and S. Sul, *Wireless Power Transfer—Principles and Engineering Explorations*. Rijeka, Croatia: InTech, 2012.

[26] J. Park, Y. Tak, Y. Kim, Y. Kim, and S. Nam, "Investigation of adaptive matching methods for near-field wireless power transfer," *IEEE Trans. Antennas Propag.*, vol. 59, no. 5, pp. 1769–1773, May 2011.

[27] W. S. Lee, W. I. Son, K. S. Oh, and J. W. Yu, "Contactless energy transfer systems using antiparallel resonant loops," *IEEE Trans. Ind. Electron.*, vol. 60, no. 1, pp. 350–359, Jan. 2013.

[28] K. Aditya and S. S. Williamson, "Design guidelines to avoid bifurcation in a series–series compensated inductive power transfer system," *IEEE Trans. Ind. Electron.*, vol. 66, no. 5, pp. 3973–3982, May 2019.

Weiyi Tang was born in Jiangsu, China, in 1991. He received the B.S. degree in automation from Central South University, Changsha, China, where he is currently working toward the Ph.D. degree in control science and engineering.

His research interests include motor control and wireless power transfer.

Qi Zhu (S'16) was born in Anhui Province, China, in 1993. He received the B.S. degree in electrical engineering and automation from Central South University, Changsha, China, in 2014, where he is currently working toward the Ph.D. degree in electrical engineering. Since December 2017, he has been a Joint Ph.D. Student at the University of Auckland, Auckland, New Zealand, funded by the China Scholarship Council.

His main research interest is wireless power transfer, including both inductive power transfer and capacitive power transfer.

Jian Yang (M'09) received the Ph.D. degree in electrical engineering from the University of Central Florida, Orlando, FL, USA, in 2008.

From 2007 to 2010, he was a Senior Electrical Engineer with Delta Tau Data Systems, Inc., Los Angeles, CA, USA.

Since 2011, he has been with Central South University, Changsha, China, where he is currently a Professor with the School of Information Science and Engineering. His main research interests include motion control, power electronics and its applications in wind energy generation systems, and photovoltaic systems.

Dongran Song received the B.S., M.S., and Ph.D. degrees from the School of Information Science and Engineering, Central South University, Changsha, China, in 2006, 2009, and 2016, respectively.

Since 2018, he has been as an Associate Professor with Central South University. From 2009 to 2013, he was an Electrical and Control Engineer with China Ming Yang Wind Power, Zhongshan, China. His research interests include wind turbines, power electronics, and renewable energy system.

Mei Su (M'19) received the B.S., M.S., and Ph.D. degrees from the School of Information Science and Engineering, Central South University, Changsha, China, in 1989, 1992, and 2005, respectively.

Since 2006, she has been a Professor with the School of Information Science and Engineering, Central South University, Changsha, China. Her research interests include matrix converter, adjustable speed drives, and wind energy conversion systems.

Runmin Zou (M'08) received the B.Eng. degree in electrical engineering and automation and the M.Eng. degree in control theory and control engineering from the Central South University (CSU), Changsha, China, in 1994 and 1997, respectively, and the Ph.D. degree in automatic control from the Ecole Centrale de Nantes, Nantes, France, in 2009.

Since 1997, he has been with the School of Automation, CSU, where he is currently a Full Professor. His teaching concerns systems structure and control and embedded systems. His research interests include linear system theory and real control applications.